Check for updates

Electronic correlations in nodal-line semimetals

Yinming Shao [1✉], A. N. Rudenko [2,3], Jin Hu [4], Zhiyuan Sun[1], Yanglin Zhu[5], Seongphill Moon[6,7], A. J. Millis[1,8], Shengjun Yuan [2], A. I. Lichtenstein[9], Dmitry Smirnov [7], Z. Q. Mao[5], M. I. Katsnelson[3] and D. N. Basov [1✉]

Dirac fermions with highly dispersive linear bands[1–3] are usually considered weakly correlated due to the relatively large bandwidths (*W*) compared to Coulomb interactions (*U*). With the discovery of nodal-line semimetals, the notion of the Dirac point has been extended to lines and loops in momentum space. The anisotropy associated with nodal-line structure gives rise to greatly reduced kinetic energy along the line. However, experimental evidence for the anticipated enhanced correlations in nodal-line semimetals is sparse. Here, we report on prominent correlation effects in a nodal-line semimetal compound, ZrSiSe, through a combination of optical spectroscopy and density functional theory calculations. We observed two fundamental spectroscopic hallmarks of electronic correlations: strong reduction (1/3) of the free-carrier Drude weight and also the Fermi velocity compared to predictions of density functional band theory. The renormalization of Fermi velocity can be further controlled with an external magnetic field. ZrSiSe therefore offers the rare opportunity to investigate correlation-driven physics in a Dirac system.

Correlated electron physics and topological Dirac and Weyl semimetals[1–3] are two frontiers of modern condensed matter research that remain largely separated. Correlation effects in Dirac systems are usually weak, with the notable exception of twisted-bilayer graphene[4]. However, correlations are anticipated to be enhanced in the recently discovered nodal-line semimetals (NLSMs)—systems that feature extended linear band-crossings along lines/loops in the Brillouin zone[2,5,6]. For non-dispersive nodal lines, the kinetic energy is completely quenched along the nodal-line direction in **k**-space ($v_{\mathrm{F},\parallel} \propto \partial\epsilon/\partial k_{\parallel} = 0$) but can remain large perpendicular to the nodal line ($v_{\mathrm{F},\perp} \propto \partial\epsilon/\partial k_{\perp} \approx 4.3\,\mathrm{eV\,\AA}$; refs. [6,7]). Nodal-line metals are thus fertile ground for exploring correlations in systems with linearly dispersing Dirac quasiparticles[8,9]. However, it has proven difficult to disentangle the experimental signatures of correlations from other factors that impact the low-energy physics of NLSMs[8–10]. An important exception is ZrSiS, where a recent high-field magnetotransport study found evidence of substantial mass enhancements on some Fermi surface sheets and a non-trivial temperature dependence of quantum oscillation amplitudes[11]. These findings were interpreted in terms of strong correlations and proximity to a quantum critical point at magnetic fields above 10 T. A pressing unresolved question is whether the correlation effects are field-induced or already present in the zero-field state in NLSMs.

Infrared spectroscopy[12,13] is an ideal probe of the nodal-line dispersion in NLSMs and also permits quantification of the strength of electronic correlations in solids[13–15]. The real part of the optical conductivity ($\sigma(\omega) = \sigma_1(\omega) + i\sigma_2(\omega)$) in NLSMs follows a distinct power-law behaviour linked to the energy dispersion of nodal lines[12,16,17]. Furthermore, the frequency-integrated intraband $\sigma_1(\omega)$—the Drude spectral weight ($\mathrm{SW_{Drude}}$)—gives a direct estimate of the optical kinetic energy of the quasiparticles[13,18,19]. The experimental SW is expressed as[18,19]

$$\mathrm{SW}(\Omega) = \frac{1}{\pi^2 \epsilon_0 c} \int_0^{\Omega} \sigma_1(\omega)\mathrm{d}\omega \qquad (1)$$

where Ω is the cutoff frequency to separate intra- and interband contributions, c is the speed of light and ϵ_0 is the permittivity in vacuum. When compared with (non-interacting) band theory calculations, $\mathrm{SW_{band}}$, the degree of reduction in spectral weight, $\mathrm{SW_{Drude}}/\mathrm{SW_{band}}$, offers a valuable probe of the correlation strength[13,15,18]. Although one must always bear in mind the other possible sources of inaccuracy inherent in density functional theory (DFT), this approach has been tested in correlated oxides and Fe-based superconductors and yields helpful results[14,15]. Finally, magneto-infrared spectroscopy enables direct access to the Fermi velocity through the dispersion of Landau-level (LL) transitions[16,20–23] and these results also can be compared to predictions of band theory.

In this Letter, we use a combination of zero-field and magneto-infrared spectroscopy to study the NLSM state in ZrSiSe. Spectroscopic signatures of prominent correlations are identified in both zero-field and magneto-optics datasets by comparison with DFT predictions. At variance with a closely related ZrSiS system[11,17], we find that ZrSiSe reveals enhanced correlation effects, even at zero magnetic field. The observed correlated state can be further controlled by a magnetic field, exhibiting strong renormalizations of Fermi velocity that are non-saturating up to 17.5 T.

We begin with a survey of the electronic band structure of ZrSiSe (Fig. 1) and discuss implications for the optical conductivity. Highly dispersive Dirac bands are apparent in the band structure obtained with DFT (see Supplementary Section II for details of the calculations). The nodal lines form a cage-like structure in momentum space (inset), in agreement with previous studies[6,7,11]. The energy offset of the Dirac nodes is small between the Γ-X and Γ-M directions, which are two cuts of the $k_z = 0$ nodal loop. The key result is displayed in Fig. 1b, where the complete nodal-line (grey) dispersion
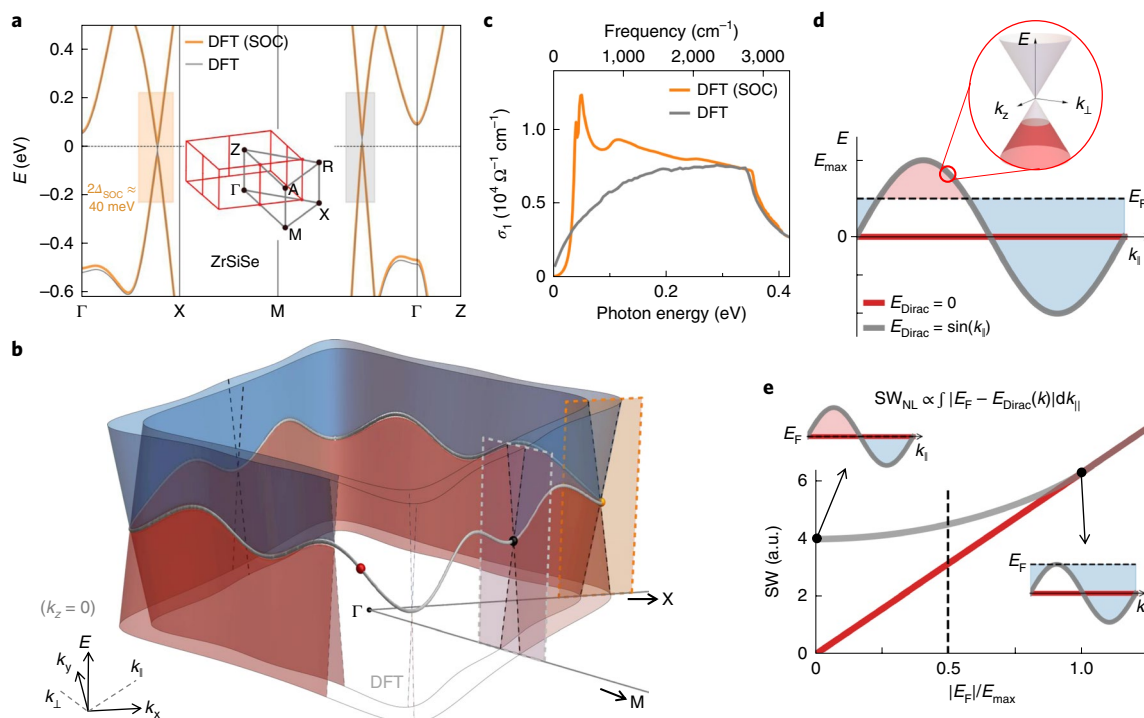
Fig. 1 | Electronic structure and optical conductivity of ZrSiSe calculated using an ab initio method. a, DFT calculations of the band structure with (orange) and without (grey) SOC. The main effect of SOC is a small gap opening of ~40 meV at the nodal line. Inset: a red cage of nodal lines in the Brillouin zone of ZrSiSe. **b**, Energy versus k_x and k_y calculation (DFT) at the $k_z = 0$ plane, showing the wave-like energy dispersion of the nodal line (grey). Grey and orange shaded planes are two-dimensional (2D) cuts along high-symmetry lines and correspond to planes in the 2D band structure plot (**a**). **c**, DFT calculations of the a–b plane interband optical conductivity of ZrSiSe. The peak near 40 meV corresponds to transitions across the SOC gap. **d**, Schematic of a sine wave dispersing nodal line and a flat nodal line along momentum $k_{\parallel}$. Note that each point on $k_{\parallel}$ represents a 2D Dirac cone in the perpendicular directions. **e**, SW_{Drude} for the dispersive (grey) and flat (red) nodal lines in **d**, showing that SW_{Drude} is reduced with flattened energy dispersion when the doping is not too large. The top and bottom insets correspond to the cases of $E_F = 0$ and $E_F = E_{max}$, respectively. For a flat nodal line, $E_{Dirac}(k) = \text{const.}$ and one recovers the known result for graphene: $SW_{Drude} \propto |E_F|$ (ref. [25]).

resembles a 'sine wave' in the energy versus k_x and k_y plot, in contrast to a hypothetical flat nodal line. Therefore, at some k_x and k_y, the Dirac points are situated below the Fermi level and at other points they are above, in contrast to the flat nodal line (Fig. 1d). These distinctions in the low-energy electronic structure lead to very different optical properties (Fig. 1c,e) in the realistic dispersive nodal lines and a hypothetical flat nodal line. As shown in Fig. 1c, DFT (grey) predicts increasing $\sigma_1(\omega)$ at low frequency as a result of dispersive nodal lines[12,16], in contrast to the frequency-independent $\sigma_1(\omega) \propto e^2/h$ (refs. [12,17]) expected for a flat nodal line. Including spin–orbit coupling (SOC) opens gaps at the Dirac points (Fig. 1a), and we notice that the low-frequency absorption is replaced by a prominent peak (Fig. 1c) in the interband optical conductivity near the SOC gap energy ($2\Delta \approx 40$ meV).

The effect of energy dispersion on SW_{Drude} can be demonstrated with a simple model, shown in Fig. 1d, where each point along the nodal-line direction $k_{\parallel}$ represents a 2D Dirac cone (inset). For a dispersive nodal line, SW_{Drude} is proportional to $\int |E_F - E_{Dirac}(k)| \mathrm{d}k_{\parallel}$ and depends on the specific dispersion of the nodal line. For a flat nodal line, the SW would be proportional to $E_F k_{\parallel}$, because the relative Fermi energy is fixed for all $k_{\parallel}$. Therefore, the flat nodal line will have a smaller SW_{Drude} than the dispersive nodal line (Fig. 1e). Interestingly, nodal-line flattening is also predicted by G_0W_0 calculations of the ZrSiSe band structure (Supplementary Fig. 5).

In Fig. 2a we plot the optical conductivity spectra extracted from temperature-dependent reflectance measurements combined with ellipsometry (see Methods and Supplementary Information for details). The real part of the optical conductivity, $\sigma_1(\omega)$, is domi-

nated by Drude free-carrier contributions at low energies. The Drude peak narrows and reveals suppressed SW at low temperature. A resonance peak appears around 380 cm^{-1} (~47 meV) at the lowest temperatures and is attributed to the interband transition across the gap triggered by SOC (Fig. 1a,c). The interband optical conductivity of ZrSiSe is nearly frequency-independent below 3,000 cm^{-1} and then develops a broad dip between 4,000 and 10,000 cm^{-1}. This latter finding is in apparent contradiction with the fact that both DFT and angle-resolved photoemission bandstructures show linear Dirac bands extending over 1 eV in bandwidth[6,7], well beyond the 0.4 eV (~3,200 cm^{-1}) anomaly in Fig. 2a. The oddity of the interband response in Fig. 2a is explained by considering the full cage-like nodal-line structure, where, at finite k_z, the horizontal nodal lines vanish, leaving only eight Dirac points (Fig. 2b). The appearance of van Hove singularities between the Dirac points leads to reduced bandwidth in certain directions (see also Supplementary Fig. 7). The suppression of optical conductivity beyond ΔE_{VHS} (black arrows, Fig. 2c,d; VHS, van Hove singularity) then follows as initial and final states for transitions are suppressed (Fig. 2d and Supplementary Section III).

To quantitatively understand the electrodynamics of ZrSiSe, we compared the optical conductivity data obtained at $T = 5$ K to the DFT-derived conductivity spectra in Fig. 2c. The calculations (orange dotted) not only reproduce the energy of the peak due to SOC but also accurately predict the overall magnitude of $\sigma_1(\omega)$. Deviations appear near 3,000–6,000 cm^{-1} (shaded blue region), where the experimental conductivity is higher than the calculated spectrum. Importantly, this difference is unlikely to reflect inaccuracies
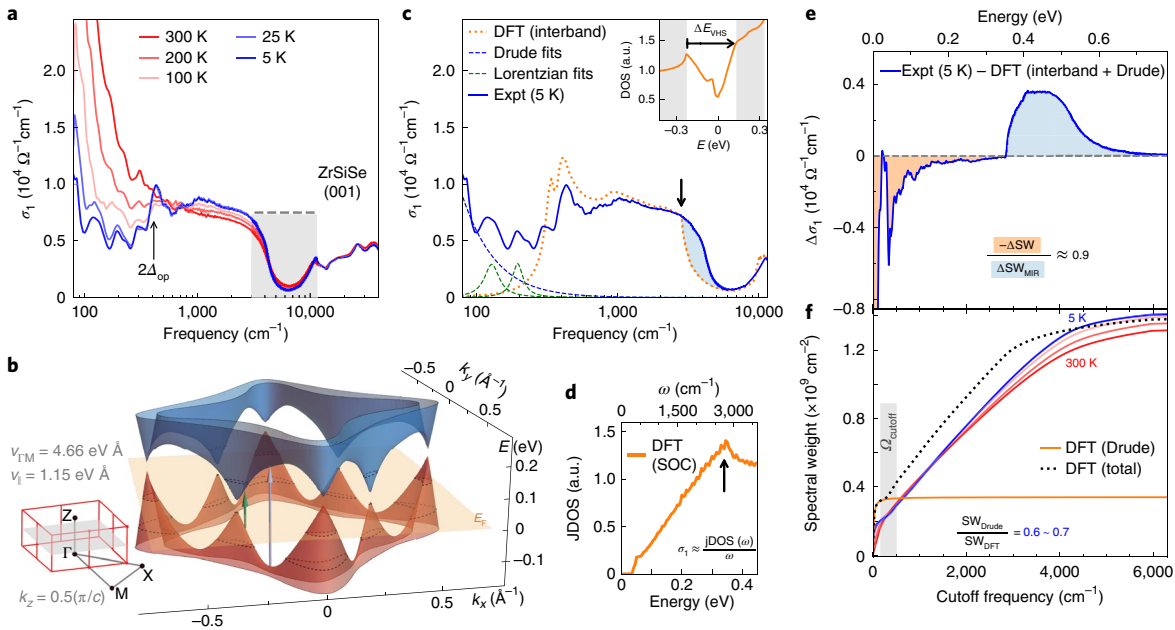
Fig. 2 | The a–b plane optical conductivity of ZrSiSe and SW analysis. a, Real part of the *a–b* plane optical conductivity $\sigma_1(\omega)$ as a function of frequency and temperature. $2\Delta_{op}$ indicates the optical gap ($2\Delta + 2E_F$). The shaded area highlights the deviation from the theoretical result for a flat nodal line (grey dashed line). **b**, Energy versus k_x and k_y calculation (DFT) at $k_z = 0.5\pi/c$ (grey plane, left panel), showing absence of the nodal line away from the $k_z = 0$ plane. Vertical arrows indicate possible interband optical transitions. Transitions with photon energy above the grey arrow will be greatly suppressed as a result of reduced density of states (DOS). **c**, Comparison of the 5 K optical conductivity with the DFT calculation (orange dotted). Blue and green dashed lines display the fit with Drude and Lorentzian formulae for the intraband part of $\sigma_1(\omega)$. The shaded blue area highlights the difference between the experiment and DFT calculations. Inset: calculated DOS showing the van Hove singularity ($\Delta E_{VHS} \approx 0.35$ eV). **d**, Calculated joint DOS (JDOS) for ZrSiSe. The black arrow indicates suppressed JDOS beyond ΔE_{VHS} and corresponds to the energy that $\sigma_1(\omega)$ is suppressed in **c** (black arrows). **e**, Calculated interband $\sigma_1(\omega)$ (DFT) subtracted from the experimental data (5 K). The lost SW at low energies (shaded orange area) is mostly recovered by the mid-infrared (MIR) peak (shaded blue area). **f**, Experimental SW integral as a function of cutoff frequency Ω, defined by equation (1) for different temperatures. The calculated (DFT with SOC) SW is shown for comparison.

of DFT, as attested by the overall excellent agreement. Rather, such deviation may originate from effects not considered in DFT, such as electronic correlations[10,19].

In correlated electron systems, there are two significant optical observables resulting from renormalization of the electronic bands[13,14,24]. One is the reduced SW_{Drude} compared with band theory and the other is renormalization of the Fermi velocity. We now explore each of these observables and find mutually consistent results.

For non-interacting metals such as copper and silver, the ratio SW_{Drude}/SW_{band} is very close to 1. In contrast, for Mott insulators, SW_{Drude}/SW_{band} is near 0, because SW_{Drude} is completely quenched while SW_{band} remains finite[13]. Mott insulators are therefore examples of the most extreme correlations. Many conducting materials derived from Mott insulators display moderate correlations with $SW_{Drude}/SW_{band} \approx 0.5$ (refs. [14,15]). In ZrSiSe, the experimental SW_{Drude} is ~3.48 eV², considerably smaller than the DFT result, $SW_{DFT} \approx 5.3$ eV² (see Supplementary Section II.A for the accuracy of the DFT calculation). We therefore obtain $SW_{Drude}/SW_{DFT} = 0.67$ and the ratio would further decrease if we were to assume an extrinsically doped system in DFT calculations (Supplementary Fig. 4). The same comparison between experiment and DFT yields $SW_{Drude}/SW_{DFT} \approx 1$ for ZrSiS. We interpret this strong suppression— approximately one-third of the experimental SW_{Drude} compared to the non-interacting theoretical value in ZrSiSe—as a signature of prominent short-range correlations[13,15,19].

Finite spectral weight below the gap is also evident in Fig. 2c, and can be included in our analysis by parametrizing the observed features with Lorentzians (green dashed lines)[17]. Even with the contributions from these subgap absorptions, the total low-energy

SW is still much smaller than band theory: $(SW_{Drude} + SW_{subgap})/SW_{DFT} = 0.71$. The enhanced SW in the range 3,000–6,000 cm⁻¹ compared to the DFT calculations is then consistent with correlation-induced SW transfer from the Drude part to the mid-infrared band. From the difference $\Delta\sigma_1 = \sigma_1(5\,K) - \sigma_1(DFT)$ plot in Fig. 2e, it is evident that the lost SW at low energies is mostly recovered by the excessive SW in the mid-infrared.

The SW obtained using equation (1) as a function of the cutoff frequency provides experimental access into the energy scales associated with the SW transfer. In Fig. 2f we plot the experimental $SW(\Omega, T)$ as a function of cutoff frequency at different temperatures and compare our findings with the DFT calculations. The total SW from DFT (black dotted line) includes both the Drude (orange line) and interband contributions, with a jump near $2\Delta_{SOC} \approx 40$ meV (grey shaded area). At low energies, SW_{Drude} is consistently smaller than the non-interacting theory (DFT total) value and we found $SW_{Drude}/SW_{DFT} \approx 0.6–0.7$. The error comes from uncertainty in the cutoff frequency Ω (grey shaded area in Fig. 2f). Consistent with the SW transfer picture above, the SW integration at energy higher than 0.8 eV matches the DFT prediction. Therefore, the electronic correlations in ZrSiSe lead to a redistribution of the low-energy SW from the Drude response to finite energies. The agreement of the mid-infrared band energy and the SW transfer energy strongly suggests that the underlying energy scale for the observed correlations effects is ~0.8 eV. We note that this energy scale is on par with the on-site Coulomb repulsion energy estimated ($U \approx 0.82–1.1$ eV) from two-orbital Hubbard models for ZrSiSe[10].

The electronic correlations effects manifest directly in renormalized Fermi velocities in both conventional and Dirac systems[24–28].
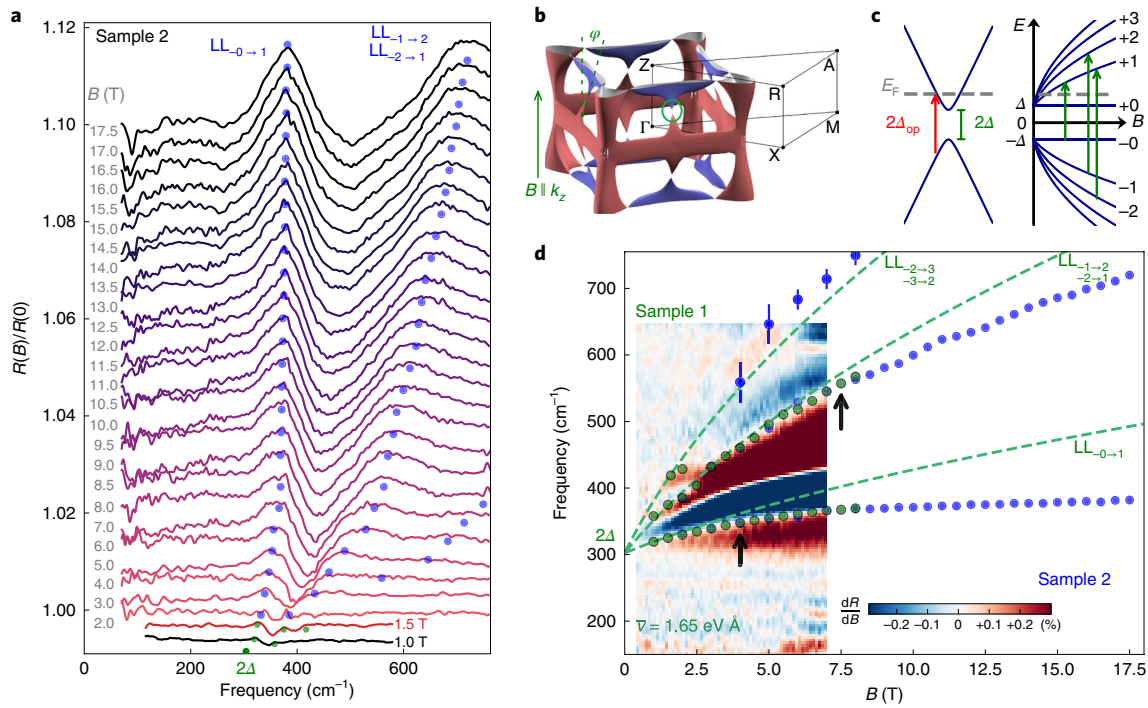
Fig. 3 | Landau-level spectroscopy of ZrSiSe. a, Magneto-reflectance $R(\omega,B)$ normalized by zero-field reflectance $R(\omega,0\,\text{T})$ up to $B = 17.5\,\text{T}$. Blue and green dots indicate dispersive peak features in $R(B)/R(0)$ from sample 2 and sample 1, respectively. **b**, Calculated 3D Fermi surface of ZrSiSe. The main contributions to the magneto-optical response come from regions with small Fermi surface (green circle, $k_z \approx 0.5\pi/c$). The local direction of the nodal line is tilted away from the magnetic field direction (k_z) by angle $\varphi \approx 22°$. **c**, Schematic showing the series of interband LL transitions (green arrows) across the massive Dirac band with gap 2Δ. **d**, Derivative $\mathrm{d}R/\mathrm{d}B$ plot (sample 1) overlaid with dispersive peak features (blue and green dots) from **a**. Fitted interband LL transitions using single-particle prediction equation (2) are shown as green dashed lines. Good agreements between theory and experiment are limited to low magnetic fields (below the black arrows). Deviations from the non-interacting theory prediction grow with increasing field and are pronounced above ~8 T. Error bars represent absolute minima and maxima in the peak positions.

The enhancement of Fermi velocity due to long-range interactions has been established both theoretically and experimentally[24–26] in graphene. However, the impact of short-range interaction on Dirac fermions is rather subtle[27]. Theory predicts that a moderate value of on-site U would reduce the Fermi velocity[27,28], in qualitative agreement with our magneto-optics data discussed below.

Magneto-infrared spectroscopy provides direct access to the averaged Fermi velocity through intra- and/or interband[22,23,29] LL transitions. The quantized LLs for Dirac bands in nodal-line materials are obtained as[16] $E_{\pm n} = \pm\sqrt{2e\hbar|n|B\bar{v}^2\cos(\phi) + \Delta^2}$, where n is the LL index, $\bar{v}$ is the average Fermi velocity perpendicular to the nodal-line direction, Δ is the half-gap and ϕ is the angle between local nodal-line direction and the magnetic field direction (Fig. 3b). Following the dipole selection rule[29,30], $\delta|n| = |n|' - |n| = \pm 1$, the transition energy is obtained as[16]

$$E_{\mathrm{T}} = \sqrt{2e\hbar|n|\bar{B}\bar{v}^2 + \Delta^2} + \sqrt{2e\hbar(|n|+1)\bar{B}\bar{v}^2 + \Delta^2} \qquad (2)$$

where $\bar{B} = B\cos(\phi)$ is the effective magnetic field parallel to the nodal-line direction[16]. This specific form implies that the 'vertical' nodal lines (Figs. 2b and 3b) contribute most to LL transitions (Supplementary Section IV). All magneto-infrared measurements discussed in this work are in Faraday geometry ($B\|k_z$, $E\perp k_z$).

Notably, the magneto-optical response effectively provides 'momentum-resolved' information for ZrSiSe due to the peculiar Fermi surface geometry (Fig. 3b). Compared to ZrSiS (Supplementary Fig. 9), the Fermi surface of ZrSiSe features nearly gapped regions along the vertical nodal line (green circle, Fig. 3b),

which results in vanishingly small Fermi pockets that are favourable for low-energy interband LL transitions. Indeed, at moderate magnetic field strength ($B < 8\,\text{T}$), we observe prominent LL transitions in ZrSiSe but not in ZrSiS, where the band filling is always high (Supplementary Fig. 9).

Figure 3a plots reflectance spectra $R(\omega,B)$ normalized by zero-field data $R(\omega,0\,\text{T})$ for ZrSiSe. A series of peaks (green and blue dots) evolve with increasing magnetic field in a notable departure from the linear law of magneto-optics followed by materials with parabolic bands[23,31]. Both the peaks[16,20] and the inflection points[21] have been used to identify resonance positions, and we found that these two methods give consistent results (Supplementary Fig. 11). We attribute the observed trends to interband LL transitions in massive Dirac systems (Fig. 3c)[16,30]. Details of the dispersion can be visualized via the derivative plot $\mathrm{d}R/\mathrm{d}B$ (ref. [16]) shown in Fig. 3d, where we also overlaid the peak features from high-field experiments in Fig. 3a.

We first discuss the low-field region ($B < 7\,\text{T}$) where the non-interacting massive Dirac equation (equation (2)) gives reasonable agreement with experimental transition energies. The main dispersive features now manifest as zero-derivative (white) regions surrounded by areas with positive (red) and negative (blue) slopes. Green dashed lines are fits obtained using equation (2) with $2\Delta = 38\,\text{meV}$ and $\bar{v} = 1.65\,\text{eV\,Å}$. Importantly, interband LL transitions can only originate from the Dirac points at finite k_z (Figs. 2b and 3b and Supplementary Section IV), where the average Fermi velocity from DFT is $v_{\mathrm{DFT}} = \sqrt{v_{\Gamma M}v_{\|}} = 2.31\,\text{eV\,Å}$ (Supplementary Fig. 10). The ratio between experimental Fermi velocity and band theory is then $\bar{v}/v_{\mathrm{DFT}} \approx 0.72 \pm 0.02$. Consistent with zero-field
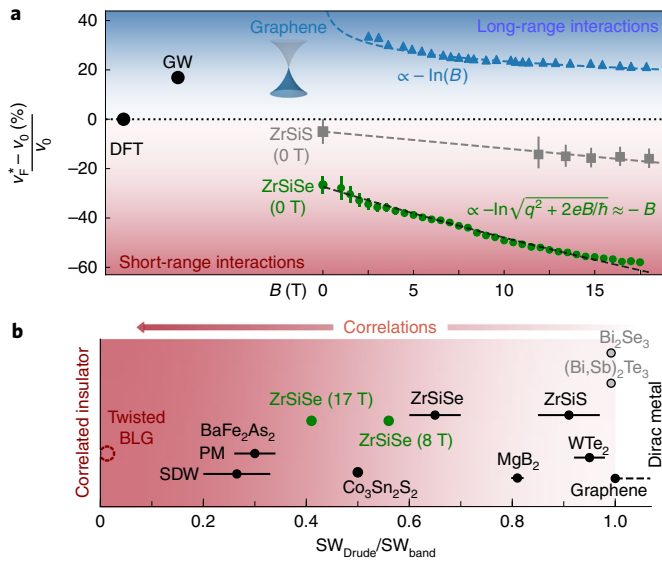
Fig. 4 | Fermi velocity and Drude SW renormalizations for various Dirac materials. a, Fermi velocity v_F^* renormalization as a function of magnetic field for ZrSiSe extracted using equation (3). v_0 is the non-interacting Fermi velocity from DFT. The GW calculation in ZrSiSe predicts a higher Fermi velocity compared to DFT (Supplementary Fig. 10). Data points for graphene are taken from LL spectroscopy experiments in ref. [32]. Data points for ZrSiS are converted from the average mass enhancement ($v_F^* \propto 1/m_\alpha + 1/m_\beta$) reported in ref. [11] (Supplementary Section V.B). The black dashed line is a fit using equation (4). **b**, Ratio of the experimental and band theory spectral weights, SW_{Drude}/SW_{band}. Metals are denoted with solid black dots. The value of the ZrSiSe data point and associated error bars are discussed in the main text. Values of SW_{Drude} and SW_{band} for other materials are obtained from $BaFe_2As_2$, paramagnetic (PM) and spin-density-wave (SDW) phase[15,19,38], MgB_2 (ref. [39]), ZrSiS (ref. [17]) (Supplementary Fig. 4), WTe_2 (ref. [40]), Bi_2Se_3 (ref. [41]), $(Bi,Sb)_2Te_3$ (refs. [23,41]) and $Co_3Sn_2S_2$ (ref. [36,37]). The dashed circle for twisted bilayer graphene (BLG) represent predictions from the observed insulating state[4]. Data points are offset vertically for clarity. Error bars represent absolute minima and maxima.

SW analysis, the average Fermi velocity also shows a reduction compared to DFT by ~30%. We remark that the slowdown of the Fermi velocity is consistent with the recent theoretical analysis of the role of on-site Hubbard interactions (U) in Dirac systems[27,28]. In a continuous Dirac model with local density–density interaction, the Fermi velocity renormalization is obtained as $v_F^*/v_0 = 1 - fU^2$ (Supplementary Section VII.D), where f is a positive constant.

In contrast to the low-field regime, the high-field region in Fig. 3d shows strikingly large discrepancies between experiment and single-particle predictions (green dashed lines). The deviations grow with increasing magnetic field and depend on the index of the LL transitions. Such behaviours resemble previous LL spectroscopy experiments in graphene, where long-range Coulomb interactions renormalize the Fermi velocity in a field-dependent way[32]. The field-dependent renormalized Fermi velocity can therefore be extracted using the experimental transition energy as[32]

$$v_F^*(B) = \sqrt{\frac{E_{01}(E_{01} - 2\Delta)}{2e\hbar B}} \tag{3}$$

where E_{01} is the energy for the $LL_{-0\to1}$ transition and $2\Delta = 38$ meV is the SOC gap determined from the fitting in Fig. 3. The resulting field-dependent $v_F^*(B)$ are shown in Fig. 4a. Compared to

similar effects in graphene (blue triangles, Fig. 4a), the field-induced changes in ZrSiSe are stronger and follow a qualitatively different scaling behaviour. Although the reduced $v_F^*(0)$ at zero field is consistent with short-ranged interactions, such pronounced field-tunability of $v_F^*(B)$ with modest magnetic field is not expected (Supplementary Section VI.B). On the other hand, the nearly linear-in-B scaling of $v_F^*(B)$ can be understood by considering the screened Coulomb interactions (Supplementary Section VII). Following the treatment of screening in ref. [33], we obtained the Fermi velocity renormalizations due to the screened Coulomb interaction[34] for a generic Dirac nodal line, $v_F^*(B)/v_0 = 1 - (e\alpha/4\hbar)\frac{1}{(\Delta/v_0+q)q}B$, where α is the effective fine structure constant ($e^2/\hbar v_0$) and q is the screening wavevector. We remark that a full description of the reduction of v_F^* and its tunability with magnetic field requires both long-range and short-range interactions (Supplementary Table 2):

$$\frac{v_F^*}{v_0} = 1 - fU^2 - \frac{e\alpha}{4\hbar}\frac{1}{(\Delta/v_0 + q)q}B \tag{4}$$

where the positive constant f and the screening wavevector q are treated as fitting parameters ($f = 1.13$ eV^{-2} and $q = 0.44$ nm^{-1}).

The characteristic field dependence of the renormalized Fermi velocity in ZrSiSe due to the screened Coulomb interaction is another manifestation of electronic correlations. Theoretically, full understanding of correlation effects due to coexisting long-range and short-range interactions is beyond perturbation theories and has only recently been addressed by quantum Monte-Carlo calculations in graphene[28].

Having demonstrated the enhanced correlations effects in ZrSiSe from both zero-field and magneto-infrared spectroscopy, we now analyse the trends of electronic correlations in Dirac materials[1,3]. In Fig. 4b, we assemble data for different Dirac metals (black dots) on a colour chart with a horizontal axis quantifying the degree of electronic correlations, SW_{Drude}/SW_{band}.

In this chart, Dirac metals with weak correlation (for example, topological insulator surface states) occupy the right-hand side, where SW_{Drude}/SW_{band} is approaching unity. The only well-characterized Dirac correlated insulator located on the left-hand side is twisted bilayer graphene, with $SW_{Drude}/SW_{band} \approx 0$. Of particular interest are systems with $SW_{Drude}/SW_{band} < 0.7$, where the correlation effects are quite prominent. We have demonstrated experimentally that ZrSiSe falls in this territory of moderate correlation strength. Note that, in a prototypical Dirac metal graphene, many-body interaction effects enhance the Fermi velocity in the vicinity of the Dirac point[25,24]. Nevertheless, SW_{Drude} remains almost unaffected[1,25] and therefore $SW_{Drude}/SW_{band} \approx 1$ (Supplementary Section II.C). The observed strongly reduced SW_{Drude} and v_F in ZrSiSe are prominent signatures of short-range interactions[15,27,28,35], and are replicated in certain other Weyl semimetals[36,37]. The delicate interplay between electron–hole symmetry and Coulomb interaction strength is predicted to lead to drastically different many-body ground states for ZrSiS and ZrSiSe, even though their electronic dispersions are very similar[8,10]. The discovery of the correlated Dirac metal state in ZrSiSe paves the way for identifying future correlated Dirac and Weyl materials using optical and magneto-optical spectroscopies.

Online content

Any methods, additional references, Nature Research reporting summaries, source data, extended data, supplementary information, acknowledgements, peer review information; details of author contributions and competing interests; and statements of data and code availability are available at https://doi.org/10.1038/s41567-020-0859-z.

References

1. Vafek, O. & Vishwanath, A. Dirac fermions in solids: from high-T_c cuprates and graphene to topological insulators and Weyl semimetals. *Annu. Rev. Condens. Matter Phys.* **5**, 83–112 (2014).
2. Armitage, N. P., Mele, E. J. & Vishwanath, A. Weyl and Dirac semimetals in three-dimensional solids. *Rev. Mod. Phys.* **90**, 015001 (2018).
3. Wehling, T., Black-Schaffer, A. & Balatsky, A. Dirac materials. *Adv. Phys.* **63**, 1–76 (2014).
4. Cao, Y. et al. Correlated insulator behaviour at half-filling in magic-angle graphene superlattices. *Nature* **556**, 80–84 (2018).
5. Fang, C., Chen, Y., Kee, H.-Y. & Fu, L. Topological nodal line semimetals with and without spin–orbital coupling. *Phys. Rev. B* **92**, 081201 (2015).
6. Schoop, L. M. et al. Dirac cone protected by non-symmorphic symmetry and three-dimensional Dirac line node in ZrSiS. *Nat. Commun.* **7**, 11696 (2016).
7. Hosen, M. M. et al. Tunability of the topological nodal-line semimetal phase ZrSiX-type materials (X = S, Se, Te). *Phys. Rev. B* **95**, 161101 (2017).
8. Rudenko, A. N., Stepanov, E. A., Lichtenstein, A. I. & Katsnelson, M. I. Excitonic instability and pseudogap formation in nodal line semimetal ZrSiS. *Phys. Rev. Lett.* **120**, 216401 (2018).
9. Mele, E. J. Dowsing for nodal lines in a topological semimetal. *Proc. Natl Acad. Sci. USA* **116**, 1084–1086 (2019).
10. Scherer, M. M. et al. Excitonic instability and unconventional pairing in the nodal-line materials ZrSiS and ZrSiSe. *Phys. Rev. B* **98**, 241112 (2018).
11. Pezzini, S. et al. Unconventional mass enhancement around the Dirac nodal loop in ZrSiS. *Nat. Phys.* **14**, 178–183 (2018).
12. Ahn, S., Mele, E. J. & Min, H. Electrodynamics on Fermi cyclides in nodal line semimetals. *Phys. Rev. Lett.* **119**, 147402 (2017).
13. Basov, D. N., Averitt, R. D., van der Marel, D., Dressel, M. & Haule, K. Electrodynamics of correlated electron materials. *Rev. Mod. Phys.* **83**, 471–541 (2011).
14. Degiorgi, L. Electronic correlations in iron-pnictide superconductors and beyond: lessons learned from optics. *New J. Phys.* **13**, 023011 (2011).
15. Qazilbash, M. M. et al. Electronic correlations in the iron pnictides. *Nat. Phys.* **5**, 647–650 (2009).
16. Shao, Y. et al. Optical signatures of Dirac nodal lines in NbAs₂. *Proc. Natl Acad. Sci. USA* **116**, 1168–1173 (2019).
17. Schilling, M. B., Schoop, L. M., Lotsch, B. V., Dressel, M. & Pronin, A. V. Flat optical conductivity in ZrSiS due to two-dimensional Dirac bands. *Phys. Rev. Lett.* **119**, 187401 (2017).
18. Millis, A. J., Zimmers, A., Lobo, R. P. S. M., Bontemps, N. & Homes, C. C. Mott physics and the optical conductivity of electron-doped cuprates. *Phys. Rev. B* **72**, 224517 (2005).
19. Schafgans, A. A. et al. Electronic correlations and unconventional spectral weight transfer in the high-temperature pnictide BaFe₂₋ₓCoₓAs₂ superconductor using infrared spectroscopy. *Phys. Rev. Lett.* **108**, 147002 (2012).
20. Chen, R. Y. et al. Magnetoinfrared spectroscopy of Landau levels and Zeeman splitting of three-dimensional massless Dirac fermions in ZrTe₅. *Phys. Rev. Lett.* **115**, 176404 (2015).
21. Akrap, A. et al. Magneto-optical signature of massless Kane electrons in Cd₃As₂. *Phys. Rev. Lett.* **117**, 136401 (2016).
22. Chen, Z.-G. et al. Two-dimensional massless Dirac fermions in antiferromagnetic AFe₂As₂ (A = Ba,Sr). *Phys. Rev. Lett.* **119**, 096401 (2017).
23. Shao, Y. et al. Faraday rotation due to surface states in the topological insulator (Bi₁₋ₓSbₓ)₂Te₃. *Nano Lett.* **17**, 980–984 (2017).
24. Elias, D. C. et al. Dirac cones reshaped by interaction effects in suspended graphene. *Nat. Phys.* **7**, 701–704 (2011).
25. Li, Z. Q. et al. Dirac charge dynamics in graphene by infrared spectroscopy. *Nat. Phys.* **4**, 532–535 (2008).
26. Yu, G. L. et al. Interaction phenomena in graphene seen through quantum capacitance. *Proc. Natl Acad. Sci. USA* **110**, 3282–3286 (2013).
27. Banerjee, S., Abergel, D. S. L., Ågren, H., Aeppli, G. & Balatsky, A. V. Universal trends in interacting two-dimensional Dirac materials Preprint at https://arxiv.org/pdf/1803.11480.pdf (2018).
28. Tang, H.-K. et al. The role of electron–electron interactions in two-dimensional Dirac fermions. *Science* **361**, 570–574 (2018).
29. Orlita, M. et al. Observation of three-dimensional massless Kane fermions in a zinc-blende crystal. *Nat. Phys.* **10**, 233–238 (2014).
30. Abergel, D. S. L., Apalkov, V., Berashevich, J., Ziegler, K. & Chakraborty, T. Properties of graphene: a theoretical perspective. *Adv. Phys.* **59**, 261–482 (2010).
31. Orlita, M. et al. Magneto-optics of massive Dirac fermions in bulk Bi₂Se₃. *Phys. Rev. Lett.* **114**, 186401 (2015).
32. Faugeras, C. et al. Landau level spectroscopy of electron–electron interactions in graphene. *Phys. Rev. Lett.* **114**, 126804 (2015).
33. Syzranov, S. V. & Skinner, B. Electron transport in nodal-line semimetals. *Phys. Rev. B* **96**, 161105 (2017).
34. Gatti, G. et al. Light-induced renormalization of the Dirac quasiparticles in the nodal-line semimetal ZrSiSe. Preprint at https://arxiv.org/pdf/1912.09673.pdf (2019).
35. Wang, J.-R., Liu, G.-Z., Wan, X. & Zhang, C. Quantum criticality of excitonic insulating transition in nodal line semimetal ZrSiS. Preprint at https://arxiv.org/pdf/1910.01450.pdf (2019).
36. Xu, Y. et al. Electronic correlations and flattened band in magnetic Weyl semimetal Co₃Sn₂S₂. Preprint at https://arxiv.org/pdf/1908.04561.pdf (2019).
37. Yang, R. et al. Magnetization-induced band shift in ferromagnetic Weyl semimetal Co₃Sn₂S₂. *Phys. Rev. Lett.* **124**, 077403 (2020).
38. Hu, W. Z. et al. Origin of the spin density wave instability in AFe₂As₂ (A = Ba,Sr) as revealed by optical spectroscopy. *Phys. Rev. Lett.* **101**, 257005 (2008).
39. Guritanu, V. et al. Anisotropic optical conductivity and two colors of MgB₂. *Phys. Rev. B* **73**, 104509 (2016).
40. Frenzel, A. J. et al. Anisotropic electrodynamics of type-II Weyl semimetal candidate WTe₂. *Phys. Rev. B* **95**, 245140 (2017).
41. Post, K. W. et al. Sum-rule constraints on the surface state conductance of topological insulators. *Phys. Rev. Lett.* **115**, 116804 (2015).

Methods

Single crystal growth. The ZrSiSe single crystals were synthesized using a chemical vapour transport method. Zr pieces, Si and Se powder with molar ratio of 1:1:1 were sealed in a quartz tube under high vacuum, with iodine as transport agent. The mixtures were heated with a temperature gradient from 1,050 °C to 950 °C for three weeks. The composition of the single crystals was confirmed by energy-dispersive X-ray spectrometry (EDS) and the measured composition was $Zr_{1.07}SiSe_{0.96}$, relatively close to the expected stoichiometric composition ZrSiSe. The typical sizes of ZrSiSe crystals were ~$2 \times 2 \times 0.1$ mm. The a–b plane was easily cleavable due to the layered structure of ZrSiSe, and the side surfaces were rough and not polishable.

Optical and magneto-optical spectroscopy. Temperature-dependent broadband reflectance spectra $R(\omega)$ (0.01 eV to 1 eV) were obtained using an in situ gold-overfilling technique in a Fourier-transform spectrometer (Bruker 66 v/S) with near-normal incidence. The high-frequency range of $R(\omega)$ was extended to ~6 eV by room- and low-temperature ellipsometry measurements[17,19] for more accurate Kramers–Kronig analysis[13]. The temperature-dependent ellipsometric measurements on ZrSiSe (0.7 eV to 6 eV) were performed using a VASE ellipsometer (J.A. Woollam) with custom-built ultra-high-vacuum chamber for two angles of incidence (60° and 75°). Reflectance spectra were calculated based on a pseudo-dielectric function obtained from ellipsometric measurements and then merged with Fourier-transform infrared spectra. Real (σ_1) and imaginary (σ_2) parts of the optical conductivity were extracted from the reflectance spectra using Kramers–Kronig analysis. The low-frequency extrapolation to d.c. conductivity was done with parameterization with Drude–Lorentzian fits (Supplementary Fig. 2). Magneto-reflectance measurements up to 8 T were measured in a Fourier-transform spectrometer (Bruker Vertex 70V) coupled to an in-house split-coil magnet (Oxford Spectromag) via light pipes. For the ratio plot, $R(B)/R(0\,T)$, a field step of 0.25 T was used, and for the derivative dR/dB plot a field step of 0.1 T was used. High-field (up to 17.5 T) magneto-reflectance measurements were performed at $T \approx 5$ K, with Faraday geometry, in the National High Magnetic Field Laboratory.

Drude SW calculation. The Drude SW, which is proportional to n/m (defined below), is directly related to the squared Fermi velocity averaged over the whole Brillouin zone (BZ):

$$
\begin{aligned}
SW_{Drude} = \omega_p^2 \quad &= 4\pi e^2 \int_{BZ} \frac{d^3 k}{(2\pi)^3} \frac{-\partial f}{\partial \epsilon} v^2(k) = 4\pi e^2 \int_{BZ} \frac{d^3 k}{(2\pi)^3} \left(\frac{-\partial f}{\partial \epsilon} \frac{\partial \epsilon}{\partial k} \right) \frac{\partial \epsilon}{\partial k} \\
&= 4\pi e^2 \int_{BZ} \frac{-\partial f}{\partial k} \frac{\partial \epsilon}{\partial k} \frac{d^3 k}{(2\pi)^3} = 4\pi e^2 \int_{BZ} \frac{\partial^2 \epsilon}{\partial k^2} f \frac{d^3 k}{(2\pi)^3} \\
&= \frac{4\pi n e^2}{m}
\end{aligned}
$$

where $f = f(\epsilon)$ is the Fermi–Dirac distribution, n is the carrier density and $m = \left(\partial^2 \epsilon / \partial k^2 \right)^{-1}$ is the effective mass. Therefore the calculation of SW_{Drude} comes directly from the ab initio calculation of the DFT band structure (velocities) (see Supplementary Section II for more details).

Data availability
Source data for Figs. 1–4 are available with the online version of this paper. All other data that support the plots within this paper and other findings of this study are available from the corresponding author upon reasonable request.

Author contributions
Y.S. and D.N.B. conceived the project. Y.S. performed the measurements and analysed the data, with help from A.N.R., Z.S., A.J.M., A.I.L. and M.I.K. A.N.R. performed the ab initio calculations with technical support from S.Y. Z.S. and A.J.M. provided theoretical support. Y.S. performed the high-field infrared measurements with help from S.M. and D.S. J.H., Y.Z. and Z.Q.M. synthesized the ZrSiSe single crystals. Y.S. and D.N.B. wrote the manuscript, with input from all co-authors.

Competing interests
The authors declare no competing interests.

Additional information
Supplementary information is available for this paper at https://doi.org/10.1038/s41567-020-0859-z.

Correspondence and requests for materials should be addressed to Y.S. or D.N.B.

Reprints and permissions information is available at www.nature.com/reprints.